PROCEEDINGS OF THE ROYAL SOCIETY A MATHEMATICAL, PHYSICAL & ENGINEERING SCIENCES

Double flow reversal in thin liquid films driven by megahertz-order surface vibration

Amgad R. Rezk, Ofer Manor, Leslie Y. Yeo and James R. Friend

Proc. R. Soc. A 2014 **470**, 20130765, published 25 June 2014

PROCEEDINGS OF THE ROYAL SOCIETY A

rspa.royalsocietypublishing.org

Research

Cite this article: Rezk AR, Manor O, Yeo LY, Friend JR. 2014 Double flow reversal in thin liquid films driven by megahertz-order surface vibration. *Proc. R. Soc. A* **470**: 20130765. http://dx.doi.org/10.1098/rspa.2013.0765

Received: 15 November 2013
Accepted: 1 May 2014

Subject Areas:
fluid mechanics, acoustics, microsystems

Keywords:
acoustic streaming, micro- and nano-scale fluid phenomena, surface acoustic waves, flow reversal

Author for correspondence:
James R. Friend
e-mail: james.friend@rmit.edu.au

Double flow reversal in thin liquid films driven by megahertz-order surface vibration

Amgad R. Rezk, Ofer Manor†, Leslie Y. Yeo and James R. Friend

Micro/Nanophysics Research Laboratory, RMIT University, Melbourne, Victoria 3000, Australia

Arising from an interplay between capillary, acoustic and intermolecular forces, surface acoustic waves (SAWs) are observed to drive a unique and curious *double* flow reversal in the spreading of thin films. With a thickness at or less than the submicrometre viscous penetration depth, the film is seen to advance *along* the SAW propagation direction, and self-similarly over time $t^{1/4}$ in the inertial limit. At intermediate film thicknesses, beyond one-fourth the sound wavelength λ_ℓ in the liquid, the spreading direction *reverses*, and the film propagates *against* the direction of the SAW propagation. The film *reverses* yet again, once its depth is further increased beyond one SAW wavelength. An unstable thickness region, between $\lambda_\ell/8$ and $\lambda_\ell/4$, exists from which regions of the film either rapidly grow in thickness to exceed $\lambda_\ell/4$ and move *against* the SAW propagation, consistent with the intermediate thickness films, whereas other regions decrease in thickness below $\lambda_\ell/8$ to conserve mass and move *along* the SAW propagation direction, consistent with the thin submicrometre films.

1. Introduction

Useful for many microfluidic applications [1,2], high-frequency sound waves ($\mathcal{O}(10–10^3\,\mathrm{MHz})$) strongly interact with fluids at the micro- to nanoscale and underpin a diverse range of complex and nonlinear phenomena, from colloidal patterning [3], chaotic advection [4] and interfacial jetting [5], to self-similar droplet generation [6] and fingering instabilities [7].

†Present address: Department of Chemical Engineering, Technion-Israel Institute of Technology, Haifa, Israel.

Royal Society Publishing

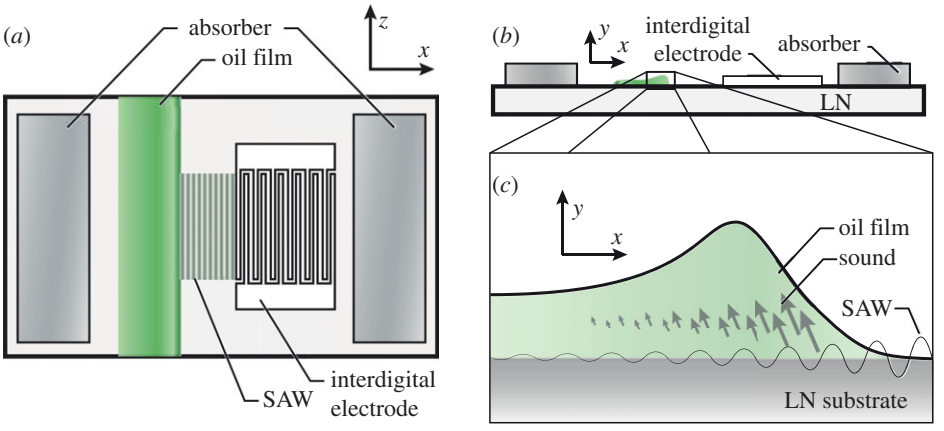

Figure 1. An oil strip is deposited on the piezoelectric substrate along a line perpendicular to the SAW propagation path, as shown from (*a*) the top and (*b*) the side. Gel absorbers, placed at either end of the device, absorb the SAW generated by the interdigital electrode, preventing edge reflections and ensuring (*c*) the deformation of the film is as a result of pure Rayleigh SAW. (Online version in colour.)

Rayleigh surface acoustic waves (SAWs) are used in a majority of these studies for their microscale wavelengths, monolithic device construction, efficient acoustic energy carriage and effective coupling of the energy into a fluid placed upon the device. Here, SAWs were found to induce rapid spreading of distinct, submicrometre to millimetre-thick oil films in an arrangement as shown in figure 1, with the film exhibiting three thickness ranges and associated reversal of flow as illustrated in figure 2. The flow was found to reverse between each of these film thickness regimes, resulting in a complex, thickness-dependent flow in which the film is observed to spread *along*, *opposite* and again *along* the SAW propagation direction depending upon its thickness.

While the thicker pair of films and a single associated flow reversal was observed in an earlier study [7], none of the remaining phenomena has been reported. The ability to form a submicrometre film, and—between the thinner pair of these three film thickness ranges—a *second* flow reversal and an associated unstable thickness region have now been discovered and found to lead to the formation of sharply defined film protrusions and depressions that bizarrely move in different directions depending on their particular thicknesses.

The behaviour is shown through analysis to be governed by a scale-dependent competition between capillary, acoustic attenuation-driven, acoustic radiation-driven and intermolecular forces. In past work, no theoretical prediction was made for the critical thicknesses at which the flow reversals occur, h_{c_1} and h_{c_2}, but predictions for these values and an explanation of the mechanisms responsible for both flow reversals, the instabilities and the thin, intermediate and thicker film behaviours are all provided here for the first time.

The paper is organized as follows. In §2, the procedure used to form and spread the thin oil films using the SAW is explained. Then, the behaviour of the film over the three thickness regimes is briefly explored in §3, from its thinnest condition, through its first critical transition to the intermediate thickness, and through the second transition to the thickest regime. This is followed by an analysis of the film as it transitions between the thickest and intermediate regimes in §4, an analysis of the unique behaviour of the thinnest film in §5 and the peculiar instability associated with the transition from this thinnest film to the intermediate regime in §6.

2. Experimental procedure

The SAW was generated using a continuous sinusoidal electrical input using a signal generator (SML01, Rhode & Schwarz, North Ryde, NSW, Australia) and amplifier (10W1000C, Amplifier

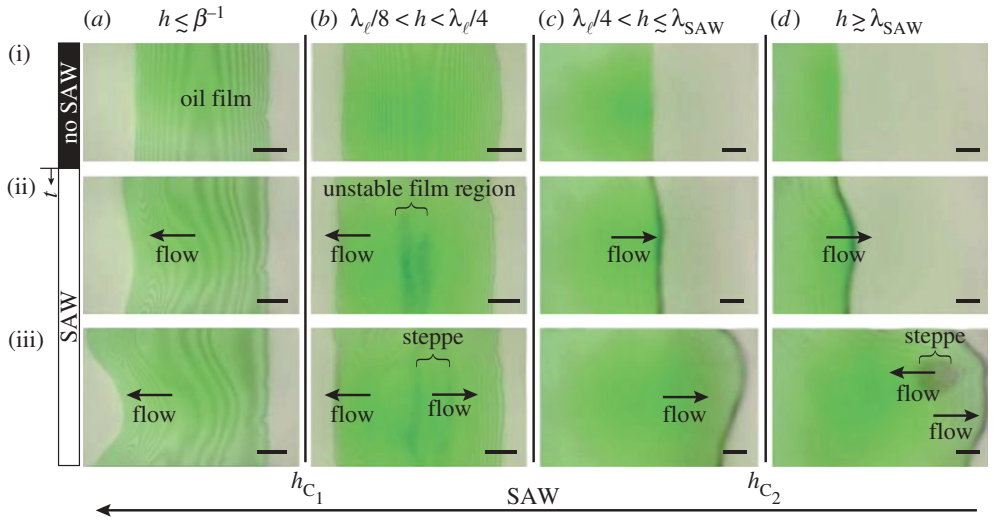

Figure 2. Sequential images of the double flow reversal phenomenon over time (along the vertical axis (i–iii)) for different initial film thicknesses (individual columns *a–d*) placed as illustrated in figure 1. The SAW propagates from right to left as indicated at the bottom of the images. Row (i) is without SAW, and rows (ii,iii) illustrate the film development owing to the SAW. If the film's maximum thickness is (*a–i*) less than or comparable to the viscous penetration length ($h \lesssim \beta^{-1}$), then the film will move in the direction of the SAW (*a*(ii,iii)). If the film is (*b*) slightly thicker ($\lambda_{SAW}/8 < h < \lambda_{SAW}/4$), then the thicker portions of the film are unstable (*b*(ii)) and grow to form steppes of thickness $h > \lambda_\ell/4$ that move in opposition to the SAW (*b*(iii)). The regions surrounding these steppes decrease in thickness below $\lambda_\ell/8$ to conserve mass and move along the SAW propagation direction (*b*(iii)). As the overall film thickness (*c*(i)) exceeds this unstable region yet remains less than one sound wavelength in the film ($\lambda_\ell/4 < h \lesssim \lambda_\ell$), it continues to flow in opposition to the SAW, but in a stable manner (*c*(ii,iii)). (*d*) Where the film thickness generally exceeds the SAW wavelength $h \gtrsim \lambda_{SAW}$, as shown by the steppe in the bottommost image (*d*(iii)), the flow direction reverses again, now in the same direction as the SAW. There are critical transition film thicknesses at which both the first and second flow reversals occur; these are denoted by h_{c_1} and h_{c_2}, respectively. All scale bars are 100 μm. (Online version in colour.)

Research, Souderton, PA) into a simple interdigital electrode composed of 42 straight electrode finger pairs formed from 175 nm Au atop 5 nm Cr. This was patterned via standard liftoff ultraviolet lithography with 50, 30 and 20 μm wide fingers and separated by gaps of similar width, leading to resonance frequencies of 19.5, 32.7 and 48.5 MHz, respectively, for the formation of Rayleigh SAW on 127.68° *Y*-rotated cut, *X*-propagating single crystal lithium niobate (LN, Roditi Ltd., London, UK). For these frequencies, the SAW wavelength λ_{SAW} is 204, 122 and 82 μm, respectively, and the sound wavelength in the fluid λ_{SAW} is 73, 44 and 29 μm, respectively. To prevent stray SAW radiation and edge reflections, we used silicone gel (α-gel, Geltec Ltd., Tokyo, Japan) along the device's edges. The input electric power was measured using a digital oscilloscope (TDS4012B, Tektronix, Beaverton, OR) with appropriate current and voltage probes. A laser Doppler vibrometer (LDV, UHF 120, Polytec GmBH, Waldbronn, Germany) was used to measure the vibration velocity *U* perpendicular to the LN surface to confirm the existence of the Rayleigh SAW at the appropriate resonance frequencies during the experiments.

As shown in figure 1*a* an oil strip was deposited on the LN substrate by carefully dipping a 0.5 mm wide polyethylene strip in a silicone oil (Sigma-Aldrich Pty. Ltd., North Ryde, NSW, Australia) reservoir, placing it in a clamp fastened to a translation stage, and 'writing' the thin oil film across the LN substrate—as a simple version of dip-pen lithography [8]—in a controlled and repeatable manner with a desired thickness dependent upon the translation speed of the polyethylene strip. The oil film width was approximately 0.5 mm for the ultrathin films and slightly wider (0.75 mm) owing to the slower writing speed for thicker films, although the slight variation in width was not observed to affect the film dynamics.

Silicone oil was used to prevent evaporation and to facilitate accurate placement and thickness, although other fluids with the requisite wettability to form thin films upon LN exhibit similar behaviour. Upon application of the SAW, the film spreads, but the spreading behaviour strongly depends on the film thickness, whether as set initially or as it develops over time.

The motion of the oil film was captured using a USB video camera (AM4023 Dino-Eye, AnMo Electronics Corp., Taipei, Taiwan) at 30 fps attached to an upright epifluorescence stereomicroscope (BXFM, Olympus, Tokyo, Japan). The film's thickness was determined using fringes formed by the incident light propagating through the film and transparent LN substrate, and filtered by a 550 ± 10 nm optical notch filter (FB550–10, ThorLabs, Newton, NJ): adjacent fringes [9], for example those visible in figures 2*a*(i) and 2*b*(i), are separated by a vertical (y-axis) distance of approximately $\Delta h \sim 225$ nm.

3. Behaviour of the surface acoustic waves-driven film

Exceptionally thin films having a thickness at or less than the viscous penetration length, $h \lesssim \beta^{-1} \equiv (\mu/\pi\rho f)^{1/2}$ [10], as exemplified in figure 2*a*, are seen to spread *along* the SAW propagation direction (figures 2*a*(ii,iii)); $f = \omega/2\pi$ is the SAW frequency and μ and ρ are the fluid viscosity and density, respectively.

Regions of the film with thicknesses between one-eighth and one-fourth the sound wavelength in the fluid ($\lambda_\ell/8 < h < \lambda_\ell/4$; figure 2*b*) are unstable (figure 2*b*(ii)). Portions of these regions quickly grow in thickness beyond $\lambda_\ell/4$ to form stable 'steppes' surrounded by the remaining fluid which thins to less than $\lambda_\ell/8$ as dictated by mass conservation (figure 2*b*(iii)). The thinner regions ($h < \lambda_\ell/8$) move along the SAW propagation direction in a manner similar to the thin films of figure 2*a*, but the steppes move in *opposition* to the SAW, representing the *first* reversal. The steppe motion corresponds to the motion of thicker, stable films with thicknesses $\lambda_\ell/4 < h \lesssim \lambda_\ell$ in figure 2*c*. Such films can nevertheless increase further in thickness [7] such that $h \gtrsim \lambda_{\mathrm{SAW}}$, as shown by the small steppe region in figure 2*d*(iii). Films possessing this greater thickness will once again move *along* the direction of the SAW—the second reversal.

4. Critical transition thickness h_{c_2} between thick and intermediate films and the associated flow reversal

(a) Thick films

Turning now to an analysis of the phenomenon, we consider films with thicknesses greater than the sound wavelength, $h \gg \lambda_\ell$, i.e. films whose behaviour is depicted in figure 2*d*. The Rayleigh SAW propagating on the substrate along the x-axis is composed of longitudinal and transverse motions of similar amplitude along the surface of the substrate, $y = 0$, possessing particle velocities given by [11]

$$\mathbf{u}|_{y=0} = (u_x, u_y)|_{y=0} = U \exp\left[\mathrm{i}(\omega t - kx) - \alpha x\right](1, -\mathrm{i}), \tag{4.1}$$

where U, k and α are the amplitude of the SAW's vibration velocity, its wavenumber, and its attenuation coefficient in the substrate, respectively. When it encounters the fluid body above the substrate, the SAW leaks its energy into the fluid to generate sound waves that propagate in the fluid at a small angle with respect to the normal to the solid–fluid interface, known as the Rayleigh angle, and with the particle velocities [11]

$$\mathbf{u}|_{y>0} = U \exp[\mathrm{i}(\omega t + \varphi) - (\alpha + \mathrm{i}k)(x + \xi y)](\xi^{-1}, 1), \tag{4.2}$$

thus resulting in the attenuation of the transverse component of the SAW.

An upper bound for the effective body force invoked by gradients in the sound field along the SAW propagation axis in the fluid [12] can be determined from an upper bound for the rate of sound attenuation along the film. We estimate this upper bound for the sound attenuation

rate by neglecting reflections of sound off the free surface of the film, so that the sound field in (4.2) is attenuated strictly owing to the SAW attenuation, a common approach [13], because its attenuation length (measured in millimetres for most fluids) is three orders of magnitude smaller than the attenuation length of sound in the film (in the range of metres) [14].

To illustrate this we note that, should we incorporate continuous reflections of sound off the free surface of the film, resulting in sound propagation along the film owing to the initial leakage of sound at the Rayleigh angle and propagation of the sound in the fluid as an acoustic waveguide between the free interface and solid substrate, the rate of attenuation of sound intensity in the film will be *reduced*. The spatial attenuation of the SAW, quantified by α in (4.1), results in the corresponding reduction in sound intensity along the film in (4.2). This reduction in intensity will then be balanced by the propagation of sound along the film and result in a reduced attenuation of sound intensity, producing a smaller effective attenuation coefficient in (4.2) compared with α. If we choose to neglect sound reflections, then we can thus safely ignore the attenuation of sound in the fluid owing to viscous and thermal effects, because the attenuation occurs at such long length scales compared with the attenuation of the SAW, the dominant effect defining our upper bound for the sound's attenuation length. The upper limit for the corresponding body force along the film at long times is then

$$F_x = \langle \rho \mathbf{u} \cdot \nabla \mathbf{u} + \mathbf{u} \nabla \cdot \rho \mathbf{u} \rangle \cdot \hat{\mathbf{x}} \approx \frac{\rho \alpha U^2 (1 + \xi^2)}{\xi^2}, \tag{4.3}$$

where $\langle \cdots \rangle \equiv (2\pi/\omega)^{-1} \int_{t=0}^{t=2\pi/\omega} \cdots \mathrm{d}t$ denotes time averaging of the quantity in the angled brackets, $\hat{\mathbf{x}}$ is the unit vector along x and $\xi \equiv [(c_{\mathrm{SAW}}/c_{\mathrm{f}})^2 - 1]^{1/2}$ in which c_{SAW} and c_{f} are the phase velocity of the wave in the solid and the fluid, respectively.

This body force generates flow—*Eckart streaming*—*along* the direction of the SAW [13,15] whose volume flux for a slender film geometry can be approximated by seeking a solution to the streamfunction ψ_{E} defined by $(u_x,\ u_y) \equiv (\partial_y \psi_{\mathrm{E}}, -\partial_x \psi_{\mathrm{E}})$ that satisfies the no-slip boundary condition at the substrate–fluid boundary,

$$\partial_y \psi_{\mathrm{E}}|_{y=0} = 0, \tag{4.4}$$

a tangential stress-free condition at the free surface of the film, which can be approximated by

$$\partial_{yy} \psi_{\mathrm{E}}|_{y=0} = 0, \tag{4.5}$$

and the equation governing conservation of momentum, subjected to the thin film approximation,

$$\partial_{yyy} \psi_{\mathrm{E}} = -\frac{F_x(x)}{\mu}. \tag{4.6}$$

Capillary contributions are ignored in the analysis above for Eckart streaming within a relatively flat film to facilitate its comparison with Rayleigh streaming, responsible in a significant part for flow in a thinner form of the film as explored in §4*b*. Solving the above by integrating (4.6), and using the boundary conditions imposed by (4.4) and (4.5), results in the following volume flux (per unit film width):

$$Q_{\mathrm{E}} = \psi|_{y=h} - \psi|_{y=0} \approx \frac{\alpha h^3 (\xi^2 + 1) \rho U^2}{3 \mu \xi^2} \tag{4.7}$$

along the direction of the SAW propagation, consistent with the motion of the steppe in figure 2*d*(iii). While such Eckart flows usually dominate large sessile drop translation experiments, in which the drops are observed to move along the SAW propagation direction [15,16], we have shown that these flows are also dominant in the film in figure 2*d*(iii) and previously in the solitary wave-like ridges in [7], as long as the thickness of these features exceed the sound wavelength ($h \gg \lambda_\ell$).

(b) Intermediate thickness films

Intermediate thickness films ($\lambda_\ell/4 < h \lesssim \lambda_\ell$; figure 2*c*), however, propagate in *opposition* to the SAW. The thicknesses are quantized to specific values [17] as dictated by the acoustic radiation pressure upon the film interface [18], discussed in §6. In our previous work, we have shown that such counterpropagating films arise owing to a drift flow induced at the outer edge of the viscous boundary layer—*Rayleigh streaming*—which has a corresponding volume flux per unit width of the film [7]:

$$Q_R \approx -\frac{U^2 h}{(12\pi f \beta^{-1} \log 2)}. \tag{4.8}$$

This directional volume flux, formed by the propagating SAW, was previously explained in detail [11]; the flow morphology in the film is also notably different to the classical vortices formed by Rayleigh streaming from a standing wave. Equating the two volume fluxes associated with Eckart streaming dominant in thick ($h \gg \lambda_\ell$) films and Rayleigh streaming dominant in intermediate thickness ($\lambda_\ell/4 < h \lesssim \lambda_\ell$) films specified by (4.7) and (4.8), respectively, then gives an order-of-magnitude estimate for the critical thickness at which the second flow reversal occurs

$$h_{c_2} \approx \left[\left(\frac{\mu}{4\pi\alpha\rho\beta^{-1}\log 2} \right) \left(\frac{c_{SAW}^2 - c_f^2}{c_{SAW}^2} \right) \right]^{1/2}. \tag{4.9}$$

Substitution of the appropriate physical properties into (4.9) gives $h_{c_2} \approx 1$–$1.5\lambda_\ell$, in good order-of-magnitude agreement with the experimental transition $h_{c_2} \sim 2.8\lambda_\ell \sim \lambda_{SAW}$ previously observed for different experimental parameter sets [7].

5. Submicrometre thin films

When the film is far thinner, on the order of or below the viscous penetration length ($h \lesssim \beta^{-1} \ll \lambda_\ell$; figure 2*a*), however, and therefore too thin to sustain sound waves [19,20], the film moves in response to a convective drift flow induced by the SAW along the substrate (i.e. (4.1)), subjected to the following conditions enforcing tangential stress continuity at the solid–fluid interface $y = 0$ and the normal stress discontinuity at the free surface $y = h$:

$$\partial_y u_x = 0 \tag{5.1}$$

and

$$2\mu \partial_y u_y = (p + \gamma \partial_{xx} h - \Pi), \tag{5.2}$$

respectively, with p, γ and Π being the hydrodynamic pressure, surface tension, and disjoining pressure, respectively.

Conservation of the local mass and momentum within the thin film is governed by the classical periodic boundary layer flow equation [19,20]

$$\frac{\mu}{\rho} \partial_y^4 \psi \approx \partial_t (\partial_y^2 \psi) + \partial_y \psi \partial_x (\partial_y^2 \psi) - \partial_x \psi \partial_y (\partial_y^2 \psi), \tag{5.3}$$

where ψ is a streamfunction satisfying $(u_x, u_y) \equiv (\partial_y \psi, -\partial_x \psi)$. This may be solved to determine the film flow in the limit of small SAW attenuation ($\alpha \to 0$) subjected to the boundary conditions stipulated by (4.1), (5.1) and (5.2). Omitting linear periodic solutions of the flow field that become negligible as $t \to \infty$ by time averaging the general solution over the SAW period ω^{-1} using a tedious mathematical procedure documented elsewhere [11], the re-dimensionalized leading order, steady volume flux $\psi|_{y=h(x)} - \psi|_{y=0}$ may then be written as

$$Q_S \approx \frac{U^2}{72\omega} \left(\frac{h}{\beta^{-1}} \right)^4 + \frac{h^3}{3\mu} (\gamma \partial_{xxx} h - \partial_x \Pi), \tag{5.4}$$

in which the first term represents the volume flux, driven directly by the drift flow for small $h(x)$ and the second term represents contributions to the fluid transport in the film from capillary,

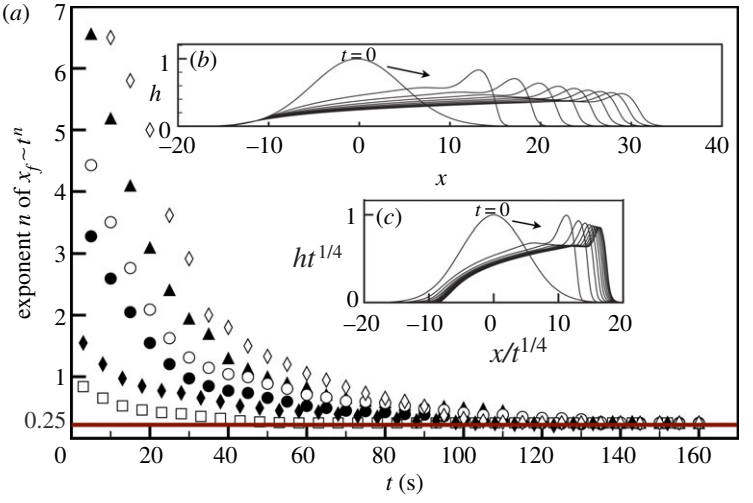

Figure 3. (*a*) The spreading velocity of the advancing film front x_f is a function of time t such that $x_f \sim t^n$; the exponent n converges to 0.25 at $t \to \infty$ for many choices of experimental parameters: open boxes $f = 48.5$ MHz, $\mu = 100$ mPa s^{-1}, $U = 0.03$ m s^{-1}; closed diamonds $f = 19.5$ MHz, $\mu = 50$ mPa s^{-1}, $U = 0.1$ m s^{-1}; filled circles $f = 32.7$ MHz, $\mu = 50$ mPa s^{-1}, $U = 0.13$ m s^{-1}; circles $f = 48.5$ MHz, $\mu = 500$ mPa s^{-1}, $U = 0.08$ m s^{-1}; filled triangles $f = 19.5$ MHz, $\mu = 100$ mPa s^{-1}, $U = 0.15$ m s^{-1}; and open diamonds $f = 19.5$ MHz, $\mu = 50$ mPa s^{-1}, $U = 0.2$ m s^{-1} describe specific test conditions, respectively. The insets show that the numerical prediction of the spatio-temporal evolution of the film (*b*) collapses in a self-similar manner (*c*) upon scaling $h \to ht^{1/4}$ and $x \to x/t^{1/4}$, which agrees well with the decay of (*a*) the experimental spreading velocity data as $x_f \to t^{1/4}$ as $t \to \infty$. The arrows in (*b*) and (*c*) indicate the direction of increasing time. (Online version in colour.)

acoustic radiation and intermolecular forces, respectively. The dynamics of the film spreading can then be obtained by imposing integral mass conservation through the kinematic condition:

$$\partial_t h = -\partial_x Q_S. \tag{5.5}$$

The dynamics of the film is then governed by a balance between the drift flow and the capillary and molecular forces in (5.4), reducing the film evolution equation given by (5.4) and (5.5) to

$$\partial_t h \approx -\frac{U^2}{18\omega}\frac{h^3}{\beta^{-4}}\partial_x h - \frac{1}{3\mu}\partial_x(h^3(\gamma\,\partial_{xxx}h - \partial_x \Pi)), \tag{5.6}$$

with a form functionally similar to those describing inertia-dominant films [21,22], suggesting that the thinnest films represented by the behaviour shown in figure 2*a* spread in the direction given by the average volume flux term in (5.4): *along* the SAW propagation direction.

The evolution of the film profile according to a numerical solution of (5.4) and (5.5) using the method of lines [23] and imposing the arbitrary initial condition

$$h(t = 0) = \cosh^{-1} x \tag{5.7}$$

and no-flux boundary conditions

$$\partial_x h = \partial_{xxx} h = 0 \qquad \text{at } x \to \pm\infty = 0 \tag{5.8}$$

for a fully wetting film is depicted in figure 3. We note that the assumption of a fully wetting film is reasonable given the small contact angle ($< 20^\circ$) of silicone oil, for which the disjoining pressure can be described by $\Pi = A/6\pi h^3$. The film spreading dynamics was insensitive to the specific choice of the Hamaker constant $A = 10^{-19}$ to 10^{-20} J. In the numerical scheme, fourth-order-centred differences were used for discretization of the spatial derivatives and Gear's method was used for integration in time. The numerical results shown in figure 3*b*,*c*

were evaluated over 4500 evenly spaced positions within a spatial domain of length 600 k^{-1}, where $k^{-1} = \lambda_{SAW}/2\pi$, using the parameters associated with the diamonds in figure 3*a* with $\rho = 1000\,\mathrm{kg\,m^{-3}}$, $\gamma = 0.021\,\mathrm{N\,m^{-1}}$ and $c_{SAW} = 3980\,\mathrm{m\,s^{-1}}$. Other choices of physical parameters provided only quantitatively different results over short timescales; the results were qualitatively similar throughout and were, regardless, quantitatively similar as $t \to \infty$.

Both the experimental data and numerical prediction for the film spreading velocity are observed in figure 3*a* to decay to a constant, non-zero value as $t \to \infty$. More specifically, the film is seen to spread in a self-similar manner, advancing as $t^{1/4}$, as indicated by both the collapse in the film evolution profile in figure 3*b* through rescaling h and x according to the similarity transformation $h \sim t^{-1/4}$ and $x_f \sim t^{1/4}$ (figure 3*c*), and by the constant asymptotic exponent, n, in $x_f \sim t^n$, to which the experimentally measured film velocity data in figure 3*a* decays as $t \to \infty$.

The capillary and intermolecular forces in the second term in (5.4), ignored in the similarity scaling, appear to only influence the shape of the spreading film, not its dynamics. Only the first term in (5.6) was retained in the derivation of the similarity scaling and plotted in figure 3; this term is associated with the drift flow. The good agreement in the prediction of the velocity of the advancing film front between the experimental and numerical results therefore suggests that the $t^{1/4}$ spreading law, and hence the spreading dynamics is governed by this boundary layer drift.

6. The critical transition thickness h_{c_1} between thin and intermediate films, and the associated thickness instability and flow reversal

We finally turn our attention to the instability apparent in experiments on films with thicknesses $\lambda_\ell/8 < h < \lambda_\ell/4$ while exposed to the SAW (figure 2*b*(ii)), corresponding to region (ii) in the phase plot given in figure 4*a*. The instability appears to be driven when the acoustic radiation pressure imparted on the free surface of the film, forcing it upwards such that the film thickness is increased to an extent that it can no longer be balanced by restoring capillary forces. This is because while radiation pressure is negligible in a sufficiently thin film ($h \lesssim \beta^{-1}$), causing it to spread solely owing to the drift flow along the direction of the SAW as governed by (5.4) and (5.5), an increase in the film thickness into the range $\lambda_\ell/8 < h < \lambda_\ell/4$ (figure 2*b*) leads to significant acoustic radiation pressure on the film, overwhelming the restoring capillary forces, in turn, driving the observed film thickness instability. We now consider a film which is sufficiently thick, so that acoustic radiation pressure effects are significant, while excluding the relatively weak contributions arising from the disjoining pressure. At the same time, this film is presumed to be sufficiently thin ($h \ll \lambda_\ell$) that Eckart streaming is weak.

The acoustic radiation pressure upon the free surface of the film, p_r, essentially arises from the reflection of the sound waves propagating in the fluid from the large acoustic impedance change at the fluid–air interface [18]. If the SAW attenuation is assumed negligible, for the sake of simplicity, the acoustic radiation pressure at the free surface of the film owing to the SAW can be written for small film thickness as [17]

$$p_r = \frac{1 + B/2A}{8} \frac{\rho_a U^2}{\cos^2(k_\ell h)\sin^2(k_\ell h)} + O(h/\lambda_\ell), \tag{6.1}$$

where B and A are the Fox and Wallace coefficients, ρ_a is the air density and $k_\ell = 2\pi/\lambda_\ell$ is the wavenumber in the fluid. It is then apparent that p_r approaches a minimum at $h = (1 + 2j)\lambda_\ell/8$ but becomes singular when $h \to 2j\lambda_\ell/8$, where $j = 0, 1, 2, \ldots$: the acoustic radiation pressure acts to define the thickness of the film at discrete intervals [17]. Analysis similar to the previous section then gives the film evolution equation

$$\partial_t h \approx -\frac{U^2}{18\omega}\frac{h^3}{\beta^{-4}}\partial_x h - \frac{1}{3\mu}\partial_x[h^3(\gamma\,\partial_{xxx}h + \partial_x p_r)]. \tag{6.2}$$

We now consider a linear stability analysis to obtain a theoretical prediction for this observed unstable film thickness range and hence the critical film thickness h_{c_1} at which the transition

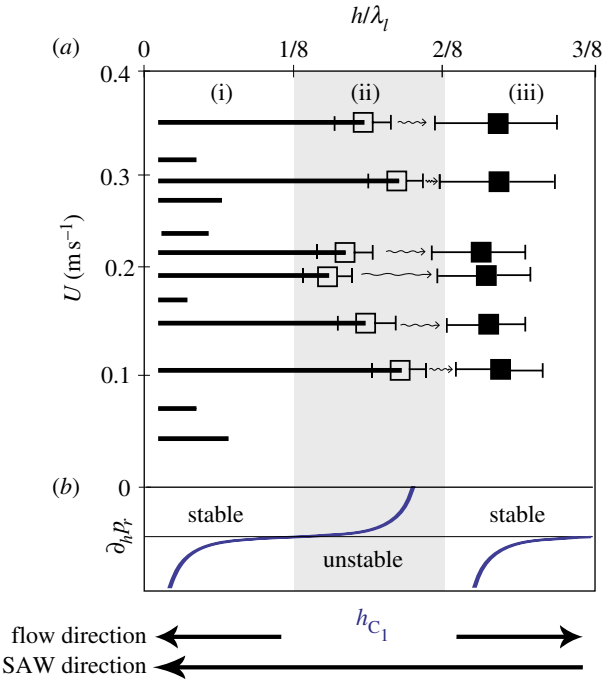

Figure 4. The experimental behaviour of the spreading film is illustrated through (*a*) a phase plot of the vibration velocity of the substrate, U, dependent upon the normalized film thickness, h/λ_ℓ, using different starting film thicknesses, oil viscosities $\mu = 50$, 100 and 500 mPa s^{-1}; and SAW frequencies 19.5, 32.7 and 48.5 MHz; for clarity, the distinction between individual parameter choices in the figure is not illustrated. The solid horizontal lines on the left in region (i) indicate the thickness range of stable films observed to move along the SAW propagation direction, as indicated by the arrow on the top of the figure and shown in figure 2*a*. The solid horizontal lines terminating at the squares with min–max error bars ($n = 5$), are for films with portions having thicknesses greater than $h/8\lambda_\ell$. These portions are unstable according to linear stability theory, as shown in (*b*): positive values of $\partial_h p_r$ correspond to an unstable film, consistent with experimental observations. Acoustic radiation pressure acts to rapidly thicken (indicated by a wavy arrow) these portions of the film to a new stable thickness, a steppe, from (open square; before SAW is applied) to (filled squares; after SAW). The film takes heights either in regions (i) or (iii) with a pronounced gap in region (ii), between the upper limit of the thinner film (open squares) and the steppe regions' thicknesses (filled squares). The portions of the film in region (i) move with the SAW, the portions of the film in region (iii) move against it. (Online version in colour.)

occurs. Briefly, we linearize the film evolution equation given by (6.2) far from the contact line. Introducing the periodic disturbance

$$h(x,t) = h_0 + \delta g(x,t), \tag{6.3}$$

to the film thickness in (6.2), in which $\delta/h_0 \ll 1$ and $g(x,t) = C\exp(\mathrm{i}nx + \sigma t) \sim \mathcal{O}(1)$, where h_0, C, n and σ are the base state film thickness, an arbitrary constant, the disturbance wavenumber and the corresponding growth rate of the film thickness, respectively. Omitting complex and small $\mathcal{O}(\delta^2)$ contributions then simplifies (6.2) to the $\mathcal{O}(\delta)$ linear equation

$$\partial_t h \approx -\frac{h_0^3}{3\mu}(\gamma\,\partial_{xxxx}h + \partial_h p_\mathrm{r}|_{h=h_0}\partial_{xx}h) + \cdots, \tag{6.4}$$

that translates to

$$\sigma g \approx -\frac{h_0^3}{3\mu}(\gamma n^4 g - \partial_h p_\mathrm{r}|_{h=h_0} n^2 g) + \cdots, \tag{6.5}$$

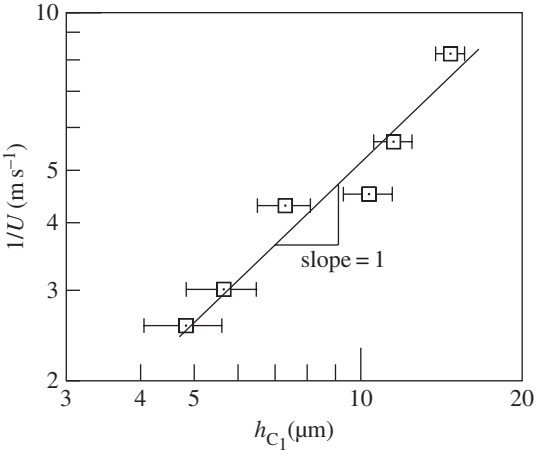

Figure 5. Correcting the linear stability prediction by accounting for the azimuthal curvature of the film in the capillary stress term of (5.2) is seen to improve the prediction of the onset of fluid instability in region (ii) of figure 4*a*.

from which we obtain the real disturbance growth rate coefficient

$$\sigma = -\frac{n^2 h_0^3 \gamma}{3\mu}\left[n^2 - \frac{1}{\gamma}\partial_h p_r|_{h=h_0}\right], \tag{6.6}$$

indicating that capillary forces act to stabilize the film ($\sigma < 1$), whereas the radiation pressure p_r acts to destabilize it ($\sigma > 1$) when σ increases with increasing h.

Substituting for p_r in (6.6) using (6.1) then reveals that the film is stable only over specific thicknesses in the range $2j\lambda_\ell/8 < h < (1+2j)\lambda_\ell/8$ ($j = 0, 1, 2, \ldots$). This behaviour is represented, in part, by the solid horizontal lines in figure 4*a*, which denote the range of stable film thicknesses found in the experiment. These primarily reside in region (i) when $h < \lambda_\ell/8$, consistent with the range predicted above with $j = 0$ and corresponding to the films whose behaviour is exemplified by figure 2*a*. In region (ii) between the predicted $j = 0$ and $j = 1$ stable regions, as illustrated by the shaded region in figure 4*b*, however, the film tends to rapidly form thicker plateaus under the action of the acoustic radiation pressure, scavenging fluid from adjacent regions to reduce the thickness of those regions, and altogether remaining within the stable thickness ranges. This is seen by the truncation of the solid horizontal lines by the open squares in figure 4*a*, with the curved arrows in the plot indicating the jump in the film thickness to the points indicated by the filled squares in the next stable region, region (iii) in figure 4*a* corresponding to the next predicted stable region $j = 1$, associated with the formation of the steppes.

In reality, the experimental data denoted by the solid horizontal lines in figure 4*a* indicate that the film remains stable even into region (ii), the region of instability predicted by linear stability theory. This is probably as a result of the omission of azimuthal γ/h curvature effects from the capillary stress term in (5.2) in the linear stability analysis, as demonstrated through a dominant balance between the azimuthal curvature and the time-averaged Reynolds stress ρU^2 that gives rise to the acoustic radiation pressure. Imposing volume conservation of the film $hL \sim 1$ in the resultant relationship $h \sim LWe^{-1}$, where L is the characteristic film length scale and $We \equiv \rho U^2 L/\gamma$ is an acoustic Weber number, explains the $h \sim 1/U$ scaling of the experimental data in figure 5 for the threshold film thickness h_{c_1} beyond which the film becomes unstable in region (ii) of figure 4.

7. Conclusion

For sufficiently thin films ($h \lesssim \beta^{-1} \ll k_l^{-1}$) that cannot sustain the propagation of acoustic waves into the liquid, the acoustic radiation pressure acting on the interface is negligible. The convective

drift generated by this dominant viscous periodic flow described by (5.6) (without the far right term, i.e. the capillary term) is then the primary mechanism that drives the spreading of these thin films in the SAW propagation direction. Films of intermediate thicknesses ($h \gtrsim k_l^{-1} \gg \beta^{-1}$), however, permit the leakage of the acoustic energy from the substrate to produce sound waves in the liquid, and are therefore influenced by an additional stress mechanism—the acoustic radiation pressure upon the film's interface—giving rise to stable and unstable regions within a film depending on its thickness. This mechanism, in addition to the drift flow, imposes a volume flux that causes the film to spread with constant velocity in opposition to the drift flow, and therefore in opposition to the SAW. For thick films and sessile drops whose characteristic thickness $h \gg k_l^{-1}$ is sufficiently large to permit viscous attenuation of the sound wave as it propagates in the liquid, long-range vortical Eckart streaming dominates and drives the fluid film to translate in the direction of the SAW propagation. The broader implications of the theoretical predictions become apparent when, for a single film possessing thicknesses across the entire range from $h \lesssim \beta^{-1}$ near the edges of the film to $h \gtrsim \lambda_{SAW}$ nearer the centre, the film moves *with*, *against* and again *with* the SAW, respectively, all the while avoiding the unstable regions predicted by the stability analysis through the formation of steppes of fluid.

The thin films, possessing a thickness of less than 1 µm, have a velocity of order 1 mm s^{-1} in the direction of the SAW. The intermediate thickness films, with thickness of approximately 20 µm, typically have velocity approximately 1 mm s^{-1} opposing the SAW propagation. Eckart-driven streaming typical of thick films have a velocity of order 100 mm s^{-1} in the direction of the SAW. If the film width is 5 mm as in our experiments, this roughly produces a volumetric flow rate of approximately 0.01, approximately 0.1 and approximately 100 mm^3 s^{-1}, respectively, for the thin, intermediate and thick films, is one to two orders of magnitude larger than typical microfluidic flows actuated by other means, including electrokinetics and magnetohydrodynamics. Driving these films via megahertz acoustics with 1 W order miniature, battery-powered circuits offers substantial versatility in that the film width is defined by the interdigital transducer's aperture, therefore, films of greater or smaller widths can also be easily achieved by changing the aperture or the nature of the transducer's construction, incorporating tapered or stepped structures.

The mechanisms driving the film spreading phenomena and the double reversal rely upon a balance between the inertial forces driving the SAW-induced convective drift flow, intermolecular forces at the edges of the film, the capillary forces present on the free surface of the film and, for cases where the film is beyond the threshold thickness h_{c_1}, the acoustic radiation pressure impinging on the free surface that acts to destabilize the film when it lies within a specific thickness range. Beyond the second critical transition h_{c_2}, when the film further increases in thickness beyond the SAW wavelength in the fluid, the attenuation then becomes sufficient to generate a body force and concomitantly, the Eckart streaming that dominates flow in the direction of the SAW propagation.

Acknowledgements. This work was performed in part at the Melbourne Centre for Nanofabrication, partly supported by the Australian National Fabrication Facility as an initiative of the Commonwealth of Australia and the Victorian Government.

Funding statement. This work was supported by a CSIRO Flagship Grant on Sensors Systems for Analysis of Aquatic Environments and Australian Research Council grants nos. DP120100013 and DP120100835. L.Y.Y. is grateful for funding from the Australian Research Council for an Australian Research Fellowship under Discovery Grant Project no. DP0985253. J.R.F. is grateful to the Melbourne Centre for Nanofabrication for a Senior Tech Fellowship and to RMIT University for a Vice-Chancellor's Senior Research Fellowship.

References

1. Friend JR, Yeo LY. 2011 Microscale acoustofluidics: microfluidics driven via acoustics and ultrasonics. *Rev. Mod. Phys.* **83**, 647–704. (doi:10.1103/RevModPhys.83.647)
2. Lin S-CS, Mao X, Huang TJ. 2012 Surface acoustic wave (SAW) acoustophoresis: now and beyond. *Lab Chip* **12**, 2766–2770. (doi:10.1039/c2lc90076a)

3. Li H, Friend JR, Yeo LY. 2008 Microfluidic colloidal island formation and erasure induced by surface acoustic wave radiation. *Phys. Rev. Lett.* **101**, 084502. (doi:10.1103/PhysRevLett.101.084502)
4. Fommelt T, Kostur M, Wenzel-Schäfer M, Talkner P, Hänggi P, Wixforth A. 2008 Microfluidic mixing via acoustically driven chaotic advection. *Phys. Rev. Lett.* **100**, 034502. (doi:10.1103/PhysRevLett.100.034502)
5. Tan MK, Friend JR, Yeo LY. 2009 Interfacial jetting phenomena induced by focused surface vibrations. *Phys. Rev. Lett.* **103**, 024501. (doi:10.1103/PhysRevLett.103.024501)
6. Taller D, Go DB, Chang H-C. 2012 Self-similar micron-size and nanosize drops of liquid generated by surface acoustic waves. *Phys. Rev. Lett.* **109**, 224301. (doi:10.1103/PhysRevLett.109.224301)
7. Rezk AR, Manor O, Friend JR, Yeo LY. 2012 Unique fingering instabilities and soliton-like wave propagation in thin acoustowetting films. *Nat. Commun.* **3**, 1167. (doi:10.1038/ncomms2168)
8. Piner RD, Zhu J, Xu F, Hong S, Mirkin CA. 1999 'dip-pen' nanolithography. *Science* **283**, 661–663. (doi:10.1126/science.283.5402.661)
9. Tolmon F, Wood J. 1956 Fringe spacing in interference microscopes. *Sci. Instrum.* **33**, 236. (doi:10.1088/0950-7671/33/6/310)
10. Morse P, Ingard K. 1986 *Theoretical acoustics*. International Series in Pure and Applied Physics. Princeton, NJ: Princeton University Press.
11. Manor O, Yeo LY, Friend JR. 2012 The appearance of boundary layers and drift flows due to high-frequency surface waves. *J. Fluid Mech.* **707**, 482–495. (doi:10.1017/jfm.2012.293)
12. Eckart C. 1948 Vortices and streams caused by sound waves. *Phys. Rev.* **73**, 68–76. (doi:10.1103/PhysRev.73.68)
13. Vanneste J, Bühler O. 2011 Streaming by leaky surface acoustic waves. *Proc. R. Soc. A* **467**, 1779–1800. (doi:10.1098/rspa.2010.0457)
14. Shiokawa S, Matsui Y, Ueda T. 1990 Study on SAW streaming and its application to fluid devices. *Jpn J. Appl. Phys.* **29**, 137–139. (doi:10.7567/JJAPS.29S1.137)
15. Brunet P, Baudoin M, Matar OB, Zoueshtiagh F. 2010 Droplet displacements and oscillations induced by ultrasonic surface acoustic waves: a quantitative study. *Phys. Rev. E* **81**, 036315. (doi:10.1103/PhysRevE.81.036315)
16. Tan M, Friend J, Yeo L. 2007 Microparticle collection and concentration via a miniature surface acoustic wave device. *Lab Chip* **7**, 618–625. (doi:10.1039/b618044b)
17. Collins DJ, Manor O, Winkler A, Schmidt H, Friend JR, Yeo LY. 2012 Atomization off thin water films generated by high-frequency substrate wave vibrations. *Phys. Rev. E* **86**, 056312. (doi:10.1103/PhysRevE.86.056312)
18. Chu B-T, Apfel RE. 1982 Acoustic radiation pressure produced by a beam of sound. *J. Acoust. Soc. Am.* **72**, 1673–1687. (doi:10.1121/1.388660)
19. Riley N. 2001 Steady streaming. *Annu. Rev. Fluid Mech.* **33**, 43–65. (doi:10.1146/annurev.fluid.33.1.43)
20. Riley N. 1998 Acoustic streaming. *Theor. Comp. Fluid Dyn.* **10**, 349–356. (doi:10.1007/s001620050068)
21. Oron A, Davis SH, Bankoff SG. 1997 Long-scale evolution of thin liquid films. *Rev. Mod. Phys.* **69**, 931. (doi:10.1103/RevModPhys.69.931)
22. Craster R, Matar OK. 2009 Dynamics and stability of thin liquid films. *Rev. Mod. Phys.* **81**, 1131–1198. (doi:10.1103/RevModPhys.81.1131)
23. Schiesser WE. 1991 *The numerical method of lines: integration of partial differential equations*, vol. 212. San Diego, CA: Academic Press.